Nuclear Science and Techniques (2024) 35:58
https://doi.org/10.1007/s41365-024-01418-0

Check for updates

Low-noise and low-power pixel sensor chip for gas pixel detectors

Zhuo Zhou[1] · Shi-Qiang Zhou[1] · Dong Wang[1] · Xiang-Ming Sun[1] · Chao-Song Gao[1] · Peng-Zhen Zhu[1] · Wei-Ping Ren[1] · Jun Liu[1] · Mu-Xian Li[1] · Chen Lian[1] · Chun-Lai Dong[1]

Received: 31 August 2023 / Revised: 6 November 2023 / Accepted: 8 November 2023 / Published online: 3 May 2024

Abstract

Topmetal-M2 is a large-area pixel sensor chip fabricated using the GSMC 130 nm CMOS process in 2021. The pixel array of Topmetal-M2 consists of pixels of 400 rows × 512 columns with a pixel pitch of 45 μm × 45 μm. The array is divided into 16 subarrays, with pixels of 400 rows × 32 columns per subarray. Each pixel incorporates two charge sensors: a diode sensor and a Topmetal sensor. The in-pixel circuit primarily consists of a charge-sensitive amplifier for energy measurements, a discriminator with a peak-holding circuit, and a time-to-amplitude converter for time-of-arrival measurements. The pixel of Topmetal-M2 has a charge input range of $\sim 0{-}3$ k e^-, a voltage output range of $\sim 0{-}180$ mV, and a charge-voltage conversion gain of $\sim 59.56\,\mu V/e^-$. The average equivalent noise charge of Topmetal-M2, which includes the readout electronic system noise, is $\sim 43.45\,e^-$. In the scanning mode, the time resolution of Topmetal-M2 is 1 LSB = 1.25 μs, and the precision is ~ 7.41 μs. At an operating voltage of 1.5 V, Topmetal-M2 has a power consumption of $\sim 49\,mW/cm^2$. In this article, we provide a comprehensive overview of the chip architecture, pixel working principles, and functional behavior of Topmetal-M2. Furthermore, we present the results of preliminary tests conducted on Topmetal-M2, namely, alpha-particle and soft X-ray tests.

Keywords Charge collection · Gas detectors · Semiconductor detectors · X-ray detectors

1 Introduction

Owing to the excellent characteristics of pixel detectors, such as high spatial resolution, high energy resolution, and fast time response, they have been widely used in high-energy physics (HEP), space science, nuclear medicine, and imaging applications [1–4]. In HEP experiments, pixel detectors are commonly used as vertex detectors for the precise position and direction measurements of particles close to the interaction point, enabling particle identification and reconstruction [5–8]. In other applications, pixel detectors are used for energy-sensitive and spatial-sensitive measurements, such as X-ray and gamma-ray imaging, and charged particle spectrometry [9–13]. Some typical examples of pixel sensors are the ALPIDE chip [14, 15] for ALICE ITS at the CERN Large Hadron Collider (LHC), the MIMOSA-28 chip [16, 17] for the STAR experiment at the BNL Relativistic Heavy Ion Collider (RHIC), the Medipix and Timepix series chips [18, 19] at CERN for particle imaging and detection, and the JadePix series chips [20–23] for the Circular Electron Positron Collider (CEPC) vertex detector.

We designed Topmetal-M2 (see Fig. 1), a large-area pixel sensor chip fabricated using the GSMC 130 nm CMOS process, in 2021. It is the second generation of Topmetal-M [24, 25] and a Topmetal series chip [25–29]. Each pixel of Topmetal-M2 combines the functionalities of two distinct types of charge sensors: a diode sensor [30–32], which uses a depletion region to generate and collect charges, and a Topmetal sensor [26, 27], which uses an exposed electrode in the top metal layer of the chip to collect charges directly. The

This work was supported by the National Key Research and Development Program of China (No. 2020YFE0202002) and the National Natural Science Foundation of China (Nos. 11875146 and U1932143).

✉ Dong Wang
dongwang@ccnu.edu.cn

✉ Xiang-Ming Sun
sphy2007@126.com

[1] PLAC, Key Laboratory of Quark and Lepton Physics (MOE), Central China Normal University, Wuhan 430079, China

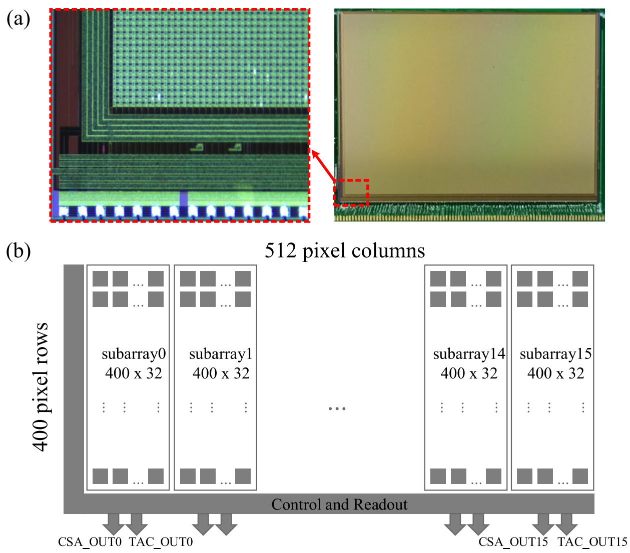

Fig. 1 (Color online) **a** Photograph of the Topmetal-M2 chip. **b** Structure diagram of Topmetal-M2

in-pixel circuit of Topmetal-M2 mainly consists of a charge-sensitive amplifier (CSA) for energy measurement, a discriminator with a peak-holding circuit, and a time-to-amplitude converter (TAC) for time-of-arrival measurements. Therefore, Topmetal-M2 can simultaneously record the position, energy, and time of arrival of the incident particles. Table 1 summarizes the main features and key parameters of Topmetal-M2 (and the first-generation chip Topmetal-M for a comparison). Here, we present a succinct comparison of Topmetal-M2 with several similar chips. In contrast to Topmetal-M, Topmetal-M2 has a lower power consumption and larger pixel pitch, although it features a more confined input range and smaller charge-voltage conversion gain. Compared with Topmetal-II^{-}, a chip employed in cosmic X-ray polarization detectors [33–35], Topmetal-M2 offers a larger sensitive area and the capability to provide time-of-arrival information. In contrast to Topmetal-CEE used for beam-monitoring applications [29], Topmetal-M2 has a lower noise level and larger sensitive area. In addition, compared with XPOL-III used for X-ray polarimetry applications [36], Topmetal-M2 has a larger gain, an extended sensitive area, and the added functionality of providing time-of-arrival information. Topmetal-M2 demonstrates potential for a wide range of applications, particularly in low-noise, low-power, and large-detection-area scenarios. For instance, it can be used as a particle track, energy, and time-of-arrival measurement detector as well as a charge collector in a time projection chamber (TPC) detector [37, 38] and a gas pixel detector [39–43]. In this article, we present a comprehensive overview of the chip architecture, the working principle of the pixel, and the functional behavior of Topmetal-M2. Additionally, we present the findings of preliminary tests conducted on Topmetal-M2, namely, an alpha-particle test in air and a soft X-ray test in a gas chamber.

2 Topmetal-M2 chip

2.1 Overall architecture

Figure 1b shows a structural diagram of Topmetal-M2. The total size of Topmetal-M2 is 19 mm × 24 mm, and the active region is approximately 18 mm × 23 mm. The pixel array contains pixels of 400 rows × 512 columns with a pixel pitch of 45 μm × 45 μm, and it is divided into 16 subarrays with 400 × 32 pixels per subarray. For each subarray, all the pixels share two analog output channels: an energy information channel (CSA channel in Fig. 2) and a time-of-arrival information channel (TAC channel in Fig. 2). The analog signals of the pixels can be driven out by digital time-division multiplexing readout

Table 1 Key parameters of Topmetal-M [25] and Topmetal-M2

Parameter	Topmetal-M	Topmetal-M2
Process	130 nm HR CMOS	130 nm CMOS
Chip size	18 mm × 23 mm	19 mm × 24 mm
Pixel array	400 × 512	400 × 512
Pixel pitch	40 μm × 40 μm	45 μm × 45 μm
Frame rate (max)	3.125 kHz	3.125 kHz
Readout mode	Scanning/single-pixel	Scanning/single-pixel
IO	32 analog output	32 analog output
Input range	0–14 k e$^-$	0–3 k e$^-$
Decay time	–	0.2–30 ms
ENC	20–50 e$^-$	43.45 e$^-$
Charge-voltage conversion gain	78.6 μV/e$^-$	59.56 μV/e$^-$
Time resolution (in scanning mode)	–	1.25 μs
Power consumption	478 mW/cm^2@3.3 V	49 mW/cm^2@1.5 V

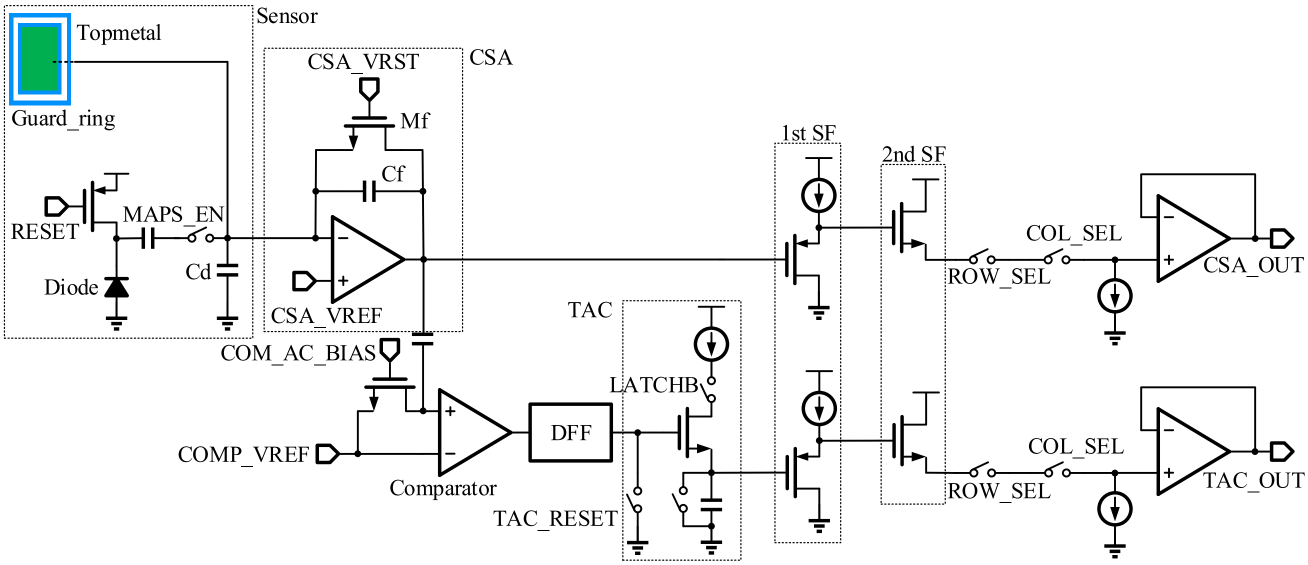

Fig. 2 Structure of a pixel unit cell in Topmetal-M2

circuitry. Topmetal-M2 can be configured in two distinct modes. In the operating mode (scanning mode), the readout circuitry controls the switching of the pixel row and column switches using a rolling shutter architecture. This enables the synchronous readout of analog signals from the 16 subarrays. Conversely, in the test mode (single-pixel mode), the readout circuitry enables the interruption of row and column switching, thereby establishing a direct connection between a specific pixel and the output buffer. The maximum clock frequency at which the readout circuitry operates is 40 MHz, which corresponds to a maximum frame rate of 3.125 kHz. The peripheral circuitry is distributed along the left and bottom edges of the chip, whereas the IO pads are positioned at the bottom. With an operating voltage of 1.5 V, the overall power consumption of Topmetal-M2 could be reduced to approximately 225 mW, thereby achieving a low power consumption of ~ 49 mW/cm^2. Compared with Topmetal-M, Topmetal-M2 achieved a reduction in power consumption by approximately 90%. However, this was achieved at the cost of a reduced input range of approximately 79% and a decrease in the charge-voltage conversion gain by approximately 24%. Nevertheless, as long as Topmetal-M2 can satisfy the requirements of scientific experiments, this tradeoff is meaningful. Therefore, Topmetal-M2 is particularly suitable for low-power, low-noise, and large-detection-area applications, such as space science experiments.

2.2 Pixel unit cell

Figure 2 shows the structure of a pixel unit cell in Topmetal-M2. This unit consists of an n-well/p-well diode sensor, a Topmetal sensor, a CSA, a comparator, a peak-holding circuit, a TAC, dual two-stage source followers, two row selection switches (ROW_SEL), two column-level column selection switches (COL_SEL), and two subarray-level analog output buffers. The layout of an individual pixel in Topmetal-M2 is depicted in Fig. 3. Each pixel is equipped with two distinct charge sensors to collect charges through two distinct mechanisms. The diode is composed of a regular octagonal n-well with a diameter of 3 μm, which has a 4 μm spacing to the surrounding square p-well. It is located in the upper-left corner of the pixel and is connected to the input of the CSA via a capacitor and a switch MAPS_EN. If the MAPS_EN switch is in the off state, the signal from the diode cannot be transmitted to the CSA, facilitating the selection of different charge sensors for various experimental purposes. The ionizing particles cross the depletion region and generate electron–hole pairs. The charges move in the depletion region under the action of an electric field and produce signals. The Topmetal sensor, which is a 14.71 μm × 40.50 μm electrode in the top metal layer, is positioned on the left side of the pixel and is directly connected to the input of the CSA. In the center of Topmetal, there is an exposed noninsulated area (green plate in Fig. 2) of 10.71 μm × 36.50 μm to collect charges directly from the surrounding space. Each Topmetal is encompassed by a guard

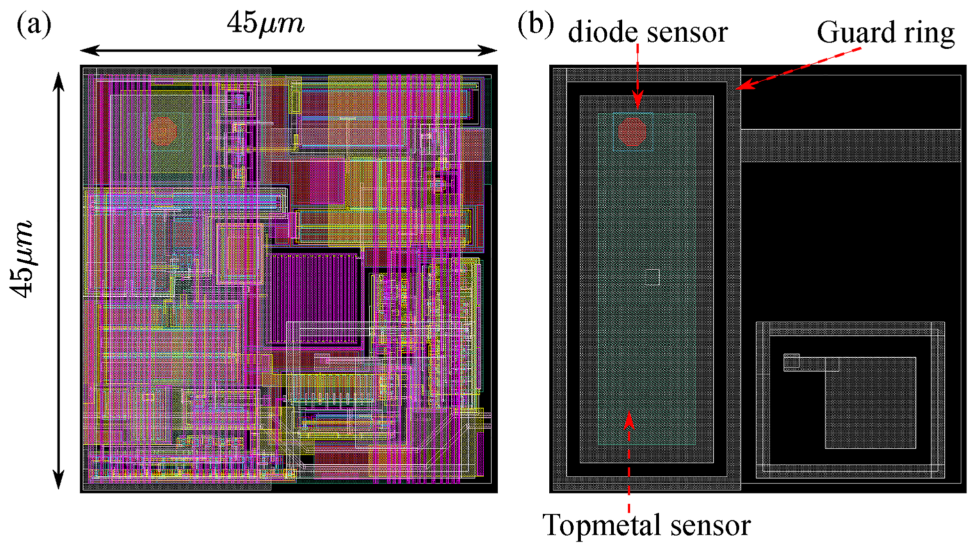

Fig. 3 (Color online) **a** Layout of a pixel unit cell in Topmetal-M2. **b** Diode sensor and Topmetal sensor

ring electrode (covered by a passivation layer) located on the same metal layer with a spacing of 1.5 μm. The width of the guard ring electrode is 1.5 μm. All the guard ring electrodes in the pixel array are connected to the same guard ring pad. The Topmetal and guard ring electrodes form a coupling capacitor C_{gt} of ~ 9.8 fF. Using the guard ring pad, a charge $Q_{in} = C_{gt} \cdot \Delta V_{in}$ can be injected into the Topmetal through C_{gt} to evaluate the performance of the pixel sensor, where ΔV_{in} represents the voltage amplitude of the negative-step pulse applied to the guard ring pad. In the scanning mode, the guard ring pad is connected to the ground. When using Topmetal sensor as a charge collection sensor, Topmetal-M2 must be used together with an ionization medium, which typically consists of a sensitive volume of gas or liquid. The charges generated in the ionization zone above Topmetal-M2 drift toward the chip surface and are directly collected by the Topmetal sensor.

The charges collected by the pixel sensor are converted into voltage signals by the CSA. The CSA, which consists of a folded cascode operational amplifier, an NMOS transistor M_f, and a feedback capacitor C_f, is one of the most crucial parts of the pixel. Figure 4 illustrates the structure of the amplifier in the CSA. Compared with the telescopic cascode architecture in the first-generation chip Topmetal-M, the folded cascode architecture has a larger common-mode input voltage swing and a larger output voltage swing, which is beneficial for our low-supply-voltage designs. The capacitor C_f is formed by the parasitic capacitance between the two metal layers, and the value is ~ 1 fF. The charge-voltage conversion gain of the CSA is $\Delta V_{out}/Q_{in} = -1/C_f$, where Q_{in} is the input charge, and ΔV_{out} is the output voltage. We use M_f as an adjustable resistor to discharge the charge accumulated in C_f. The decay time constant of the CSA output signal is $\tau = R_f \cdot C_f$, where R_f denotes the equivalent resistance of M_f. By modifying the gate voltage of M_f, we can adjust the

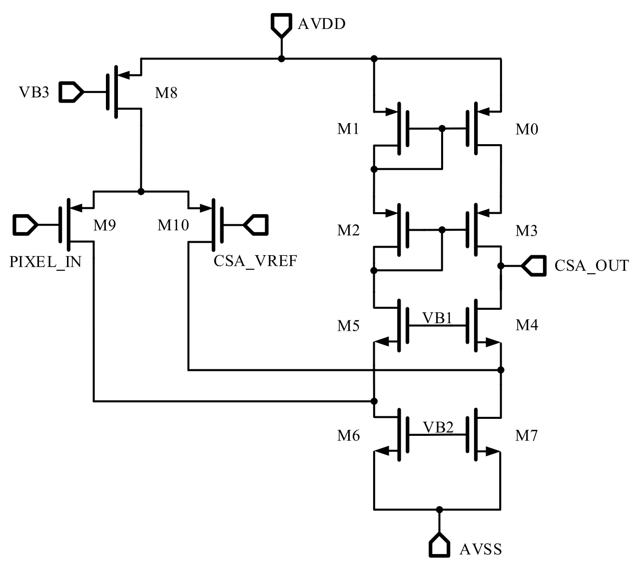

Fig. 4 Structure of the operational amplifier in the CSA

value of R_f to achieve the desired decay time of the CSA output signal.

The CSA output is divided into two channels: CSA and TAC. In the CSA channel, the CSA output is connected to two-stage source followers. The first-stage source follower isolates the CSA from the switches, whereas the second-stage source follower enhances the driving capability of the output. Each column shares a common COL_SEL connected to all the ROW_SELs within the same column. Similarly, all the COL_SELs within the same subarray are connected to an analog output buffer. ROW_SELs and COL_SELs are controlled by the readout circuitry. In the TAC channel, the CSA output is connected to a comparator via a coupling capacitor. Assuming that the LATCHB switch turns on at time T_{on} and the pixel sensor receives the charges generated by the incident particle at time T_{arrival} (arrival time of the particle), the output of the comparator transitions to a high state after a short delay time T_{delay}. The peak-holding circuit stores the output state of the comparator and initiates the charging of the capacitor in the TAC, resulting in an increasing output voltage with a fixed slope. The size of the charging current is controlled by the bias voltage of the current source in the TAC. Subsequently, the LATCHB switch turns off at time T_{off}, and the charging time T_{charge} of the capacitor can be determined from the output voltage of the TAC. The arrival time T_{arrival} can be calculated using the equation $T_{\text{arrival}} = T_{\text{off}} - T_{\text{charge}} - T_{\text{delay}}$, where T_{off}, T_{charge}, T_{delay} are known (see more details in [25]). When the TAC output is read out, the output of the peak-holding circuit and the capacitor in the TAC are reset by the switch TAC_RESET.

3 Pixel performance

3.1 CSA channel

To evaluate the basic performance of Topmetal-M2, comprehensive chip tests were conducted under ambient air and room temperature conditions. As the readout circuitry employs a rolling shutter architecture, an excessively high clock frequency (rapid pixel switching) can have a detrimental effect on the output signal quality. To ensure the optimal signal quality, the clock frequency of the chip readout circuitry was set to 20 MHz (corresponding to 640 μs per frame). Furthermore, a signal generator was utilized to apply a square-wave pulse with a peak-to-peak amplitude of ΔV to the guard ring pad of the chip. To study the performance of individual pixels, the chip was configured to operate in the single-pixel mode, enabling us to focus on a fixed pixel. As shown in Fig. 5, the CSA_VRST voltage was set to $V_{\text{CSA\_VRST}} = 750\,\text{mV}$, and the square-wave pulse amplitude was set to $\Delta V = 50\,\text{mV}$. The CSA output is a pulse signal with a rise time of $\sim 30\,\mu\text{s}$ and a decay time of $\sim 3.5\,\text{ms}$. Moreover, Fig. 6 illustrates the correlation between the CSA_VRST voltage and decay time for five different pixels. By adjusting the value of the CSA_VRST voltage, the decay time of the CSA output signal can be varied within a range of approximately 0.2–30 ms. The observed discrepancies in decay time among the pixels can be ascribed to two primary factors: the influence of the parasitic resistance on the CSA_VRST voltage of each pixel and the device mismatch in the CMOS process. Figure 7 shows the I/O dynamic range of the CSA for five different pixels. The charge-voltage conversion gain is $\sim 59.56\,\mu\text{V}/\text{e}^-$. Within the input charge range of ~ 0–$3\,\text{k e}^-$, the pixels exhibit a favorable linear response to the input pulse signal, resulting in a CSA output voltage range of ~ 0–$180\,\text{mV}$. A reduction in the operating voltage

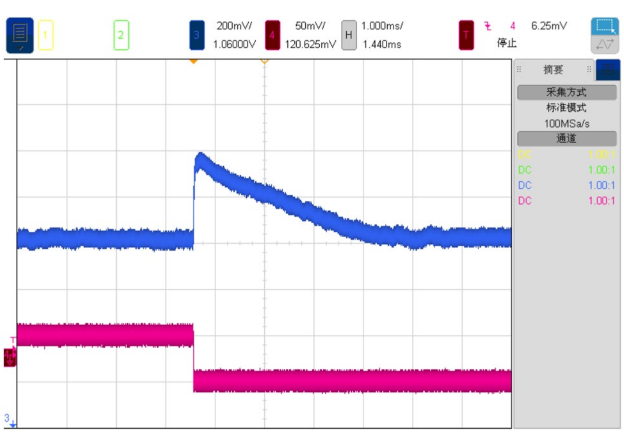

Fig. 5 (Color online) Input square-wave pulse (in pink) and CSA output pulse signal (in blue) of a pixel. (Note that, owing to the design of the readout electronics, the actual output value of the CSA is half of the value displayed by the oscilloscope. The same situation occurs for the TAC output in both Fig. 9 and Fig. 11)

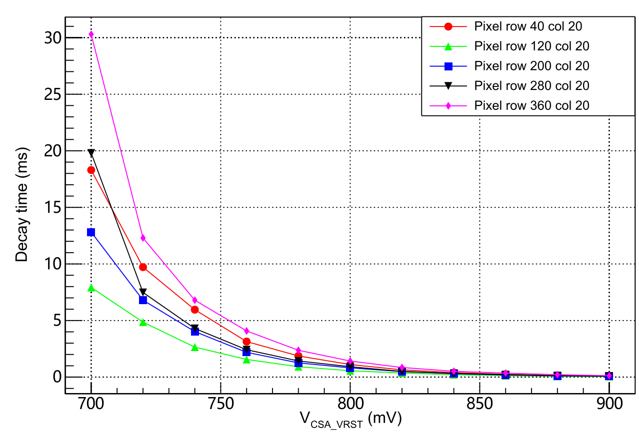

Fig. 6 (Color online) Relationship between CSA_VRST voltage and decay time for five different pixels

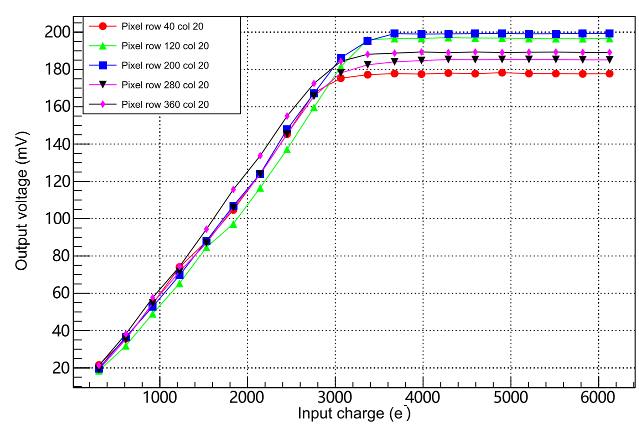

Fig. 7 (Color online) Input/output dynamic range for five different pixels

resulted in a decrease in the output swing of the amplifier, and the cascaded source followers limited the output swing. We observed discrepancies in the saturation levels among the pixels, which can be attributed to two primary factors. The first is the device mismatch in the CMOS process and the second is the effect of the parasitic resistance on the CSA bias voltage of each pixel.

To analyze the noise performance of Topmetal-M2, a square-wave pulse with an amplitude of 50 mV was applied to the guard ring pad. The CSA_VRST voltage was set to 750 mV. The CSA output was sampled using a 12-bit ADC with a dynamic range from −1 V to 1 V. The primary source of noise within a pixel channel is the CSA amplifier. The noise of a pixel channel can be characterized as the root mean square (RMS) noise voltage at the output divided by the gain of the CSA, resulting in the equivalent noise charge (ENC) given by $Q_{\text{in}} \cdot V_{\sigma}/V_{\mu}$, where V_{μ} represents the mean value of the output pulse signals, and V_{σ} represents the standard deviation. Figure 8 shows the noise distribution of all 204,800 pixels, and Gaussian fitting provides an average value of ~ 5.3 ADC count (equivalent to ~ 43.45 e^{-}). Note that this noise value encompasses the contribution from the electronic readout system.

3.2 TAC channel

In this section, we present the test results of the TAC channel for Topmetal-M2 operating in both the single-pixel and scanning modes. A signal generator was used to apply a square-wave pulse with a peak-to-peak amplitude of 50 mV as the input signal. The CSA_VRST voltage was set to 750 mV. When the LATCHB switch was turned off at time T_{off}, the TAC output voltage gradually decreased instead of remaining constant, as expected, owing to the leakage current of the reset MOS. All the pixels shared a common LATCHB pad, and it was not possible to read the TAC output voltages of all the pixels simultaneously. To solve this problem, the LATCHB switch was maintained continuously on, and the charging of the capacitor was halted using the TAC_RESET switch. Compared with Topmetal-M, Topmetal-M2 offers two TAC reset methods. The first method is a global reset, in which all the pixels are reset simultaneously using TAC_RESET (global). The second method is a local reset, where the reset signal TAC_RESET (local) generated by the readout circuitry resets the previous pixel while reading out the current pixel.

As shown in Fig. 9, the falling edge of the input signal (T_{arrival}) occurs between T_{on} and T_{off}. The TAC output voltage increases with a constant slope of K_{charge}. When TAC_RESET turns on at time T_{off}, the TAC output voltage transitions from $V_{\text{TAC\_OUT}}$ to the baseline level. A 12-bit ADC with a dynamic range of −1 V to 1 V was used to sample the TAC output voltage. Assuming that the saturation value of the TAC output voltage is $V_{\text{TAC\_OUT\_full}}$, which corresponds to the maximum charging time $T_{\text{charge\_full}}$, the time resolution can be calculated using $1\,\text{LSB} = T_{\text{charge\_full}}/(V_{\text{TAC\_OUT\_full}}/2 \cdot 2^{12})$. The time measurement range of the TAC is from 1 LSB to full-scale $T_{\text{charge\_full}}$. The precision of the TAC depends on its linearity and the resolution of the ADC. The temporal resolution of a TAC largely depends on its charging current. Increasing the charging current can enhance the time resolution but reduce the time measurement range. However, excessively high charging currents can easily cause the TAC to saturate. Therefore, the TAC must be read out and reset in time after a signal event occurs. The readout time depends on the time required to scan the chip frame. Therefore, selecting an appropriate charging current that fulfills the test requirements is crucial. As the TAC reset period of a pixel in the scanning mode is 640 μs, it is necessary to ensure that $T_{\text{charge\_full}} \geq 640$ μs. First, we conducted a chip test in the single-pixel mode.

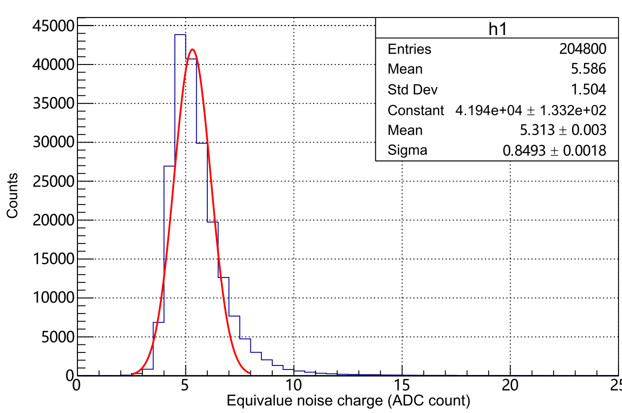

Fig. 8 Noise distribution of all 204,800 pixels

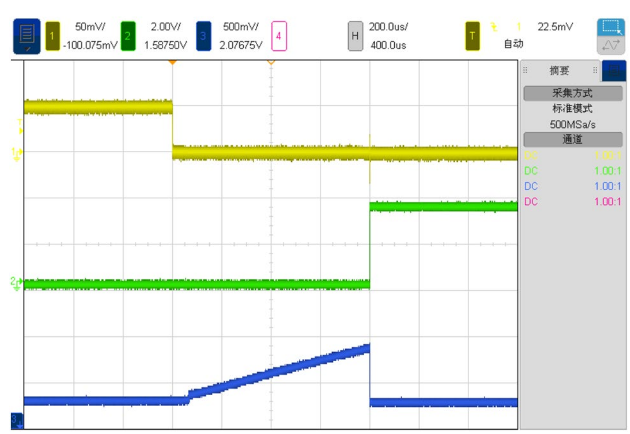

Fig. 9 (Color online) Input square-wave pulse (in yellow), TAC reset signal (in green), and TAC output signal (in blue) of a pixel (Topmetal-M2 in single-pixel mode)

We maintained $T_{\mathrm{off}} - T_{\mathrm{arrival}} = T_{\mathrm{charge}} + T_{\mathrm{delay}} = 650.00\,\mu\mathrm{s}$ as a constant and obtained $K_{\mathrm{charge}} = 460.81\,\mathrm{V/s}$; thus, the time resolution is $1\,\mathrm{LSB} = 1.06\,\mu\mathrm{s}$. The distribution of $V_{\mathrm{TAC\_OUT}}$ is shown in Fig. 10, and the time measurement precision is $\sim 6.55\,\mu\mathrm{s}$. Subsequently, we conducted a chip test in the scanning mode. As shown in Fig. 11, using a square-wave pulse as the input signal, the TAC output of all the pixels responded to this signal. We equated $T_{\mathrm{off}} - T_{\mathrm{arrival}}$ to 200.00 μs, 400.00 μs, 600.00 μs and obtained $K_{\mathrm{charge}} = 390.20\,\mathrm{V/s}$; hence, the time resolution is $1\,\mathrm{LSB} = 1.25\,\mu\mathrm{s}$. Figure 12 shows the distribution of $V_{\mathrm{TAC\_OUT}}$ with $T_{\mathrm{off}} - T_{\mathrm{arrival}} = 600.00\,\mu\mathrm{s}$; the time measurement precision is $\sim 7.41\,\mu\mathrm{s}$. Note that all the parameter values were obtained from a test chip. Different chips may have varying parameter values owing to differences in the chip production process and other conditions. Therefore, it was necessary to calibrate each chip individually.

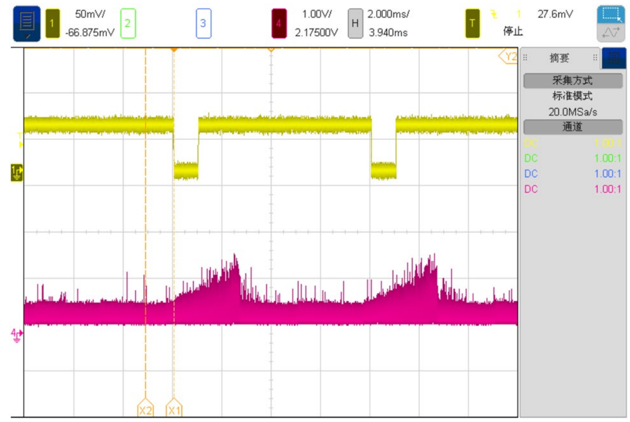

Fig. 11 (Color online) Input square-wave pulse (in yellow), and TAC output signal (in pink) of a subarray channel (Topmetal-M2 in scanning mode)

4 Test and result

4.1 Alpha-particle test

In Topmetal-M2, each pixel contains two types of sensors: a diode sensor and a Topmetal sensor. Both sensors were tested and confirmed to function appropriately. This article presents the test results of a Topmetal sensor. An alpha-particle test on Topmetal-M2 was conducted in ambient air at room temperature. Figure 13a shows the platform used for the alpha-particle test. We utilized a ^{241}Am source, which predominantly emits 5.4 MeV alpha particles, to ionize air. As shown in Fig. 13b, two metal plates were positioned parallel to Topmetal-M2 with a spacing of 20 mm. The upper metal plate served as the cathode, whereas the lower metal plate served as the anode. The electric field strength between the metal plates is approximately 500 V/cm (1000 V over a $\sim$ 2 cm air gap). The ^{241}Am source was placed on top of the upper metal plate. A square hole matching the size of Topmetal-M2 was present in the middle of the lower metal plate to allow Topmetal-M2 to receive the charges generated by the alpha particles.

As alpha particles pass through the air, they ionize the gas and generate a charge. Subsequently, the charges are attracted to the surface of Topmetal-M2 under the action of an electric field and collected by the Topmetal sensor of each pixel. We can observe the electron clouds generated by the alpha particles imaged using Topmetal-M2. Figure 14 shows two typical tracks of the alpha particles obtained in air. The particle trajectory on the pixel sensor can be observed, with the brightest portion representing the location at which the alpha particles deposited most of their energy. The signal cluster amplitude was determined by summing the amplitude values of all the fired pixels within a signal cluster.

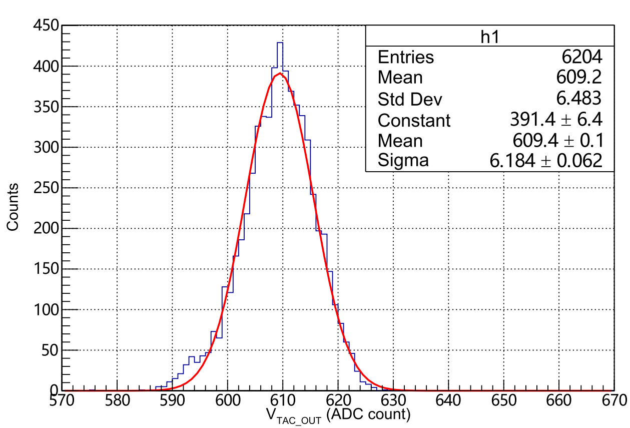

Fig. 10 Time measurement precision of a pixel (Topmetal-M2 in single-pixel mode)

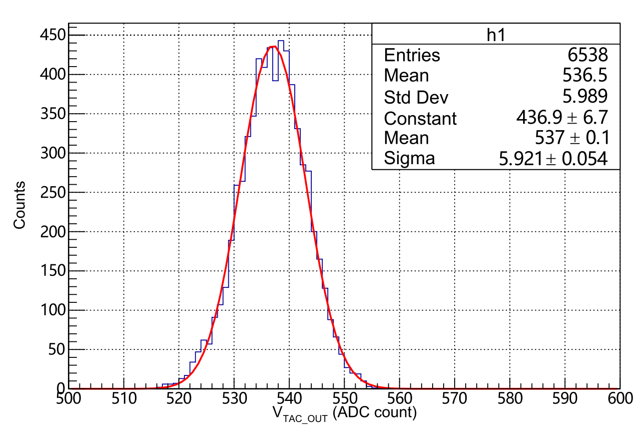

Fig. 12 Time measurement precision of a pixel (Topmetal-M2 in scanning mode)

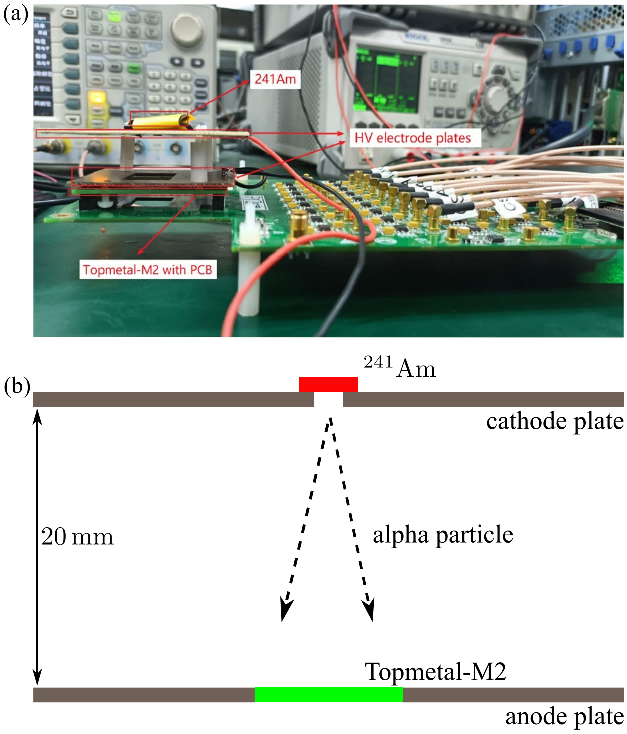

Fig. 13 (Color online) **a** Platform for the alpha-particle test. **b** Structure and principle of the test

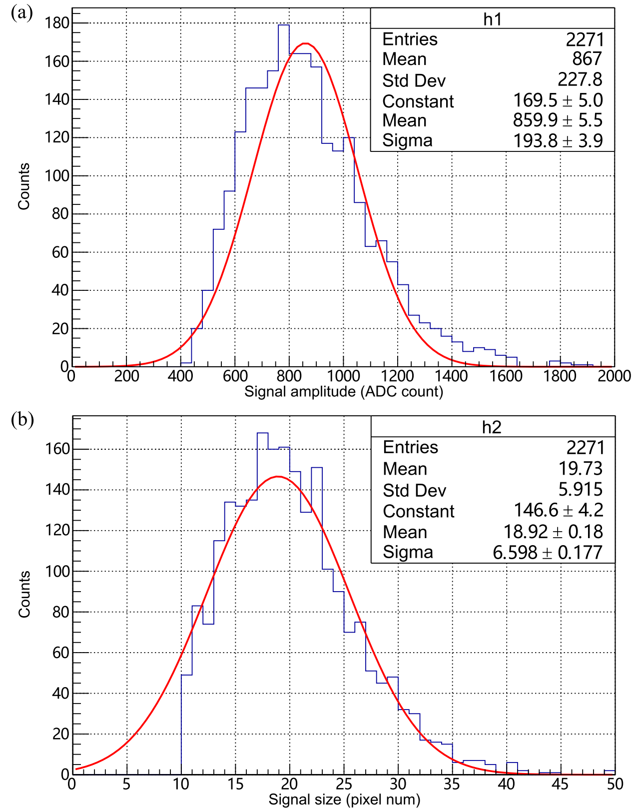

Fig. 15 Result of alpha-particle test. **a** Distribution of signal cluster amplitude. **b** Distribution of signal cluster size

Figure 15a shows the distribution of the signal cluster amplitude, and Gaussian fitting reveals the mean value of ~ 860 ADC count. The signal cluster size is defined as the number of fired pixels within a signal cluster. Figure 15b shows the distribution of the signal cluster size, with a mean value of ~ 19 pixels.

4.2 Soft X-ray test

A soft X-ray test was conducted on Topmetal-M2 in a gas chamber at room temperature. Figure 16a shows the platform of the X-ray test, where Topmetal-M2 was positioned within a sealed gas chamber and connected to a front-end electronics (FEE) board via pin headers. The chamber was filled with a mixture of helium and dimethyl ether (DME) in a ratio of 30:70 to serve as the working gas. As depicted in Fig. 16b, the chamber space can be approximately divided into three regions: electron drift, electron multiplication, and charge collection. A gas microchannel plate (GMCP) was employed as the electron multiplier in the electron multiplication region. The GMCP has a thickness of 300 μm, a microhole diameter of 50 μm, and a hole spacing of 60 μm. The distance between the cathode and the upper surface of the GMCP was 10 mm, whereas the distance between the

Fig. 14 (Color online) **a b** Two typical tracks of alpha particles obtained in air

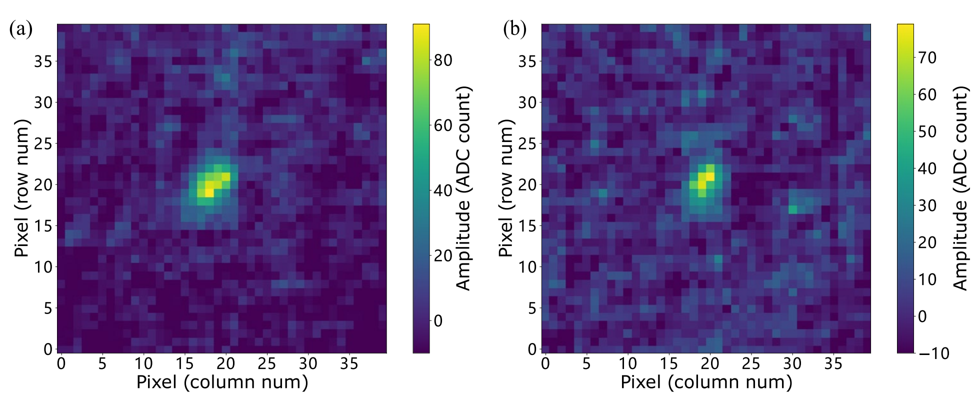

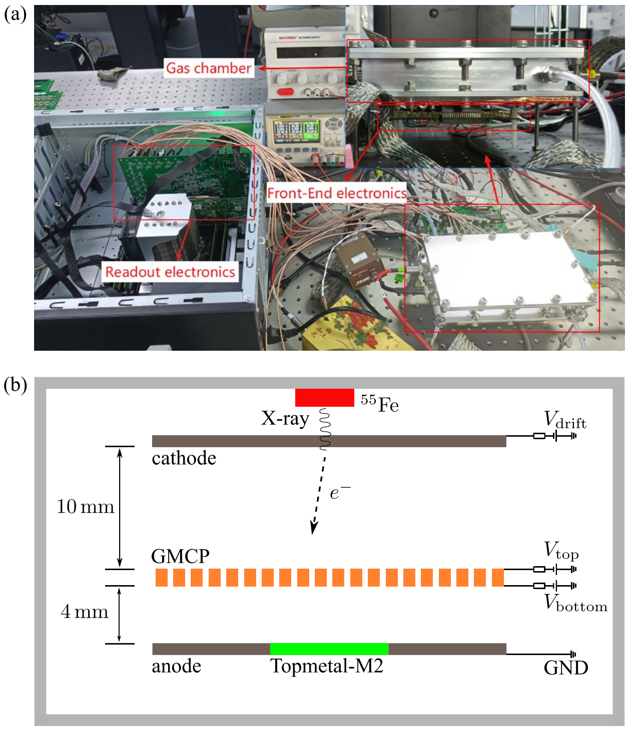

Fig. 16 (Color online) **a** Platform for the soft X-ray test. **b** Structure and principle of the test

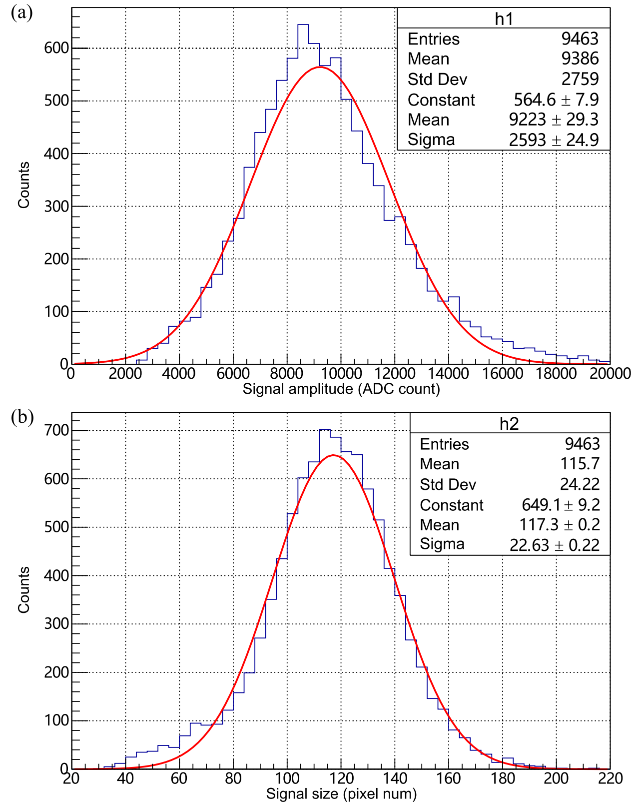

Fig. 18 Result of the soft X-ray test. **a** Distribution of signal cluster amplitude. **b** Distribution of signal cluster size

lower surface of the GMCP and the chip was 4 mm. The cathode voltage was set to $V_{drift} = -3600$ V, the upper surface voltage of the GMCP was $V_{top} = -1840$ V, the lower surface voltage of the GMCP was $V_{bottom} = -600$ V, and the anode was connected to the ground. Consequently, the electric field strength is 1.76 kV/cm in the electron drift region, 41.3 kV/cm in the electron multiplication region, and 1.5 kV/cm in the charge collection region.

An ^{55}Fe source emitting X-rays with an energy of 5.9 keV was positioned above the cathode. Through the photoelectric effect, these incident X-rays interact with the gas molecules within the electron drift region, leading to their conversion into photoelectrons. These electrons subsequently move to the upper surface of the GMCP and enter the channels through the small orifices. Within these channels, a cascade multiplication of the initial electrons occurs, known as electron gas-avalanche multiplication, resulting in the generation of a significant number of secondary electrons. These secondary electrons exit the channels from the lower surface of the GMCP and are collected by Topmetal-M2 in the anode. Figure 17 shows the photoelectron tracks of the X-rays obtained in a gas mixture of He:DME (30:70).

Fig. 17 (Color online) **a**, **b** Two typical photoelectron tracks of X-rays obtained in a gas mixture of He:DME (30:70)

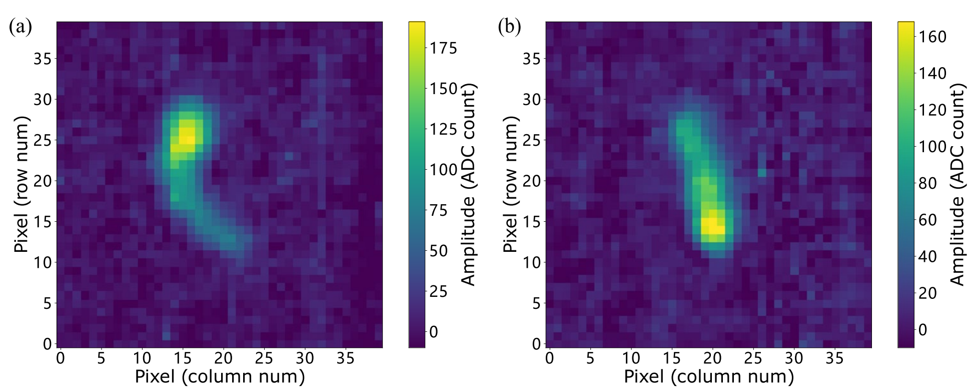

The ionization track of the photoelectrons within the gas chamber was measured. Figure 18a shows the distribution of the signal cluster amplitude, and Gaussian fitting reveals the mean value of ~ 9223 ADC count. Figure 18b shows the distribution of the signal cluster size with a mean value of ~ 117 pixels.

5 Conclusion

In this article, we introduced Topmetal-M2, a pixel sensor chip that amalgamates the functionalities of diode and Topmetal sensors. We described the chip's architecture, the working principle of its pixels, and its functional behavior. Furthermore, we presented the results of preliminary tests, namely, an alpha-particle test in air and a soft X-ray test in a gas chamber. The pixel array of Topmetal-M2 contained pixels of 400 rows × 512 columns with a pixel pitch of $45\,\mu\text{m} \times 45\,\mu\text{m}$. The array is divided into 16 subarrays, each comprising pixels of 400 rows × 32 columns. The in-pixel circuit of Topmetal-M2 predominantly encompasses a CSA channel for energy measurements and a TAC channel for time-of-arrival measurements. Therefore, Topmetal-M2 can simultaneously record the position, energy, and time-of-arrival information of the incident particles. Topmetal-M2 exhibits a charge input range of $\sim 0{-}3\,\text{k}\,\text{e}^-$, a voltage output range of $\sim 0{-}180\,\text{mV}$, and a charge-voltage conversion gain of $\sim 59.56\,\mu\text{V}/\text{e}^-$. The average ENC of Topmetal-M2, which includes the noise from the readout electronic system, is $\sim 43.45\,\text{e}^-$. In the scanning mode, Topmetal-M2 achieves a time resolution of $1\,\text{LSB} = 1.25\,\mu\text{s}$, with a time measurement precision of $\sim 7.41\,\mu\text{s}$. When operating at a voltage of $1.5\,\text{V}$, Topmetal-M2 has a power consumption of $\sim 49\,\text{mW}/\text{cm}^2$. Owing to these good performance characteristics, Topmetal-M2 demonstrates significant potential for a range of applications, particularly in scenarios that demand low noise, low power consumption, and a large detection area.

Author Contributions All authors contributed to the study conception and design. Material preparation, data collection and analysis were performed by Zhuo Zhou, Shi-Qiang Zhou and Dong Wang. The first draft of the manuscript was written by Zhuo Zhou and all authors commented on previous versions of the manuscript. All authors read and approved the final manuscript.

Data Availability The data that support the findings of this study are openly available in Science Data Bank at https://cstr.cn/31253.11.sciencedb.j00186.00416 and https://doi.org/10.57760/sciencedb.j00186.00416.

Declarations

Conflict of interest The authors declare that they have no Conflict of interest.

References

1. N. Wermes, Pixel detectors for particle physics and imaging applications. Nucl. Instrum. Methods Phys. Res. Sect. A **512**, 277–288 (2003). https://doi.org/10.1016/S0168-9002(03)01905-3
2. N. Wermes, Pixel Detectors for Charged Particles. Nucl. Instrum. Methods Phys. Res. Sect. A **604**, 370–379 (2009). https://doi.org/10.1016/j.nima.2009.01.098
3. P. Delpierre, A history of hybrid pixel detectors, from high energy physics to medical imaging. JINST **9**, C05059 (2014). https://doi.org/10.1088/1748-0221/9/05/C05059
4. W. Snoeys, Monolithic pixel detectors for high energy physics. Nucl. Instrum. Methods Phys. Res. Sect. A **731**, 125–130 (2013). https://doi.org/10.1016/j.nima.2013.05.073
5. The ALICE Collaboration, K. Aamodt, A.A. Quintana et al., The ALICE experiment at the CERN LHC. JINST **3**, S08002 (2008). https://doi.org/10.1088/1748-0221/3/08/S08002
6. The ATLAS. Collaboration, G. Aad, E. Abat et al., The ATLAS experiment at the CERN large hadron collider. JINST **3**, S08003 (2008). https://doi.org/10.1088/1748-0221/3/08/S08003
7. The CMS. Collaboration, S. Chatrchyan, G. Hmayakyan et al., The CMS experiment at the CERN LHC. JINST **3**, S08004 (2008). https://doi.org/10.1088/1748-0221/3/08/S08004
8. The LHCb Collaboration, A. A. Alves Jr, L. M. A. Filho, et al., The LHCb detector at the LHC. JINST **3**, S08005 (2008). https://doi.org/10.1088/1748-0221/3/08/S08005
9. J. Jakubek, Semiconductor pixel detectors and their applications in life sciences. JINST **4**, P03013 (2009). https://doi.org/10.1088/1748-0221/4/03/P03013
10. J. Jakubek, A. Cejnarova, T. Holy et al., Pixel detectors for imaging with heavy charged particles. Nucl. Instrum. Methods Phys. Res. Sect. A **591**, 155–158 (2008). https://doi.org/10.1016/j.nima.2008.03.091
11. R. Bellazzini, G. Spandre, M. Minuti et al., Direct reading of charge multipliers with a self-triggering CMOS analog chip with 105k pixels at 50 μm pitch. Nucl. Instrum. Methods Phys. Res. Sect. A **566**, 552–562 (2006). https://doi.org/10.1016/j.nima.2006.07.036
12. Y. Chen, H. Wang, S. Zhang et al., Hi'CT: a pixel sensor-based device for ion tomography. Nucl. Sci. Tech. **34**, 111 (2023). https://doi.org/10.1007/s41365-023-01251-x
13. Y. Chen, H. Wang, S. Zhang et al., Hi'CT: a pixel sensor-based device for ion tomography. Nucl. Sci. Tech. **34**, 111 (2023). https://doi.org/10.1007/s41365-023-01251-x
14. M. Mager, ALPIDE, the monolithic active pixel sensor for the ALICE ITS upgrade. Nucl. Instrum. Methods Phys. Res. Sect. A **824**, 434–438 (2016). https://doi.org/10.1016/j.nima.2015.09.057
15. G.A. Rinella, The ALPIDE pixel sensor chip for the upgrade of the ALICE Inner Tracking System. Nucl. Instrum. Methods Phys. Res. Sect. A **845**, 583–587 (2017). https://doi.org/10.1016/j.nima.2016.05.016
16. I. Valin, C. Hu-Guo, J. Baudot et al., A reticle size CMOS pixel sensor dedicated to the STAR HFT. JINST **7**, C01102 (2012). https://doi.org/10.1088/1748-0221/7/01/C01102
17. C.-A. Reidel, C. Schuy, C. Finck et al., Response of the Mimosa-28 pixel sensor to a wide range of ion species and energies. Nucl. Instrum. Methods Phys. Res. Sect. A **1017**, 165807 (2021). https://doi.org/10.1016/j.nima.2021.165807
18. R. Ballabriga, M. Campbell, X. Llopart, Asic developments for radiation imaging applications: The medipix and timepix family. Nucl. Instrum. Methods Phys. Res. Sect. A **878**, 10–23 (2018). https://doi.org/10.1016/j.nima.2017.07.029
19. X. Llopart, R. Ballabriga, M. Campbell et al., Timepix, a 65k programmable pixel readout chip for arrival time, energy and/or

photon counting measurements. Nucl. Instrum. Methods Phys. Res. Sect. A **581**, 485–494 (2007). https://doi.org/10.1016/j.nima.2007.08.079
20. Y. Zhang, H. Zhu, L. Zhang et al., Charge collection and non-ionizing radiation tolerance of CMOS pixel sensors using a 0.18m CMOS process. Nucl. Instrum. Methods Phys. Res. Sect. A **831**, 99–104 (2016). https://doi.org/10.1016/j.nima.2016.03.031
21. L. Chen, H. Zhu, X. Ai et al., Characterization of the first prototype CMOS pixel sensor developed for the CEPC vertex detector. Radiat Detect Technol Methods **3**, 45 (2019). https://doi.org/10.1007/s41605-019-0124-0
22. Y. Zhou, Y. Lu, Z. Wu et al., Highly compact digital pixel structures developed for the CEPC vertex detector. Nucl. Instrum. Methods Phys. Res. Sect. A **980**, 164427 (2020). https://doi.org/10.1016/j.nima.2020.164427
23. S. Dong, P. Yang, Y. Zhang et al., Design and characterisation of the JadePix-3 CMOS pixel sensor. Nucl. Instrum. Methods Phys. Res. Sect. A **1048**, 167967 (2023). https://doi.org/10.1016/j.nima.2022.167967
24. J. Liu, Z. Zhou, D. Wang et al., Prototype of single-event effect localization system with CMOS pixel sensor. Nucl. Sci. Tech. **33**, 136 (2022). https://doi.org/10.1007/s41365-022-01128-5
25. W. Ren, W. Zhou, B. You et al., Topmetal-M: A novel pixel sensor for compact tracking applications. Nucl. Instrum. Methods Phys. Res. Sect. A **981**, 164557 (2020). https://doi.org/10.1016/j.nima.2020.164557
26. M. An, C. Chen, C. Gao et al., A low-noise CMOS pixel direct charge sensor, Topmetal-II-. Nucl. Instrum. Methods Phys. Res. Sect. A **810**, 144–150 (2016). https://doi.org/10.1016/j.nima.2015.11.153
27. C. Gao, G. Huang, X. Sun, Topmetal-II-: A direct charge sensor for high energy physics and imaging applications. JINST **11**, C01053 (2016). https://doi.org/10.1088/1748-0221/11/01/C01053
28. H. Wang, Z. Wang, C. Gao et al., Design and tests of the prototype beam monitor of the CSR external-target experiment. Nucl. Sci. Tech. **33**, 36 (2022). https://doi.org/10.1007/s41365-022-01021-1
29. J. Liu, C. Gao, H. Wang et al., Design and preliminary characterization of a novel silicon charge sensor for the gaseous beam monitor at the CSR external-target experiment. Nucl. Instrum. Methods Phys. Res. Sect. A **1047**, 167786 (2023). https://doi.org/10.1016/j.nima.2022.167786
30. G. Deptuch, G. Claus, C. Colledani et al., Development of monolithic active pixel sensors for charged particle tracking. Nucl. Instrum. Methods Phys. Res. Sect. A **511**, 240–249 (2003). https://doi.org/10.1016/S0168-9002(03)01801-1
31. R. Turchetta, J.D. Berst, B. Casadei et al., A monolithic active pixel sensor for charged particle tracking and imaging using standard VLSI CMOS technology. Nucl. Instrum. Methods Phys. Res. Sect. A **458**, 677–689 (2001). https://doi.org/10.1016/S0168-9002(00)00893-7
32. G. Deptuch, M. Winter, W. Dulinski et al., Simulation and measurements of charge collection in monolithic active pixel sensors. Nucl. Instrum. Methods Phys. Res. Sect. A **465**, 92–100 (2001). https://doi.org/10.1016/S0168-9002(01)00361-8
33. H. Wang, D. Wang, R. Chen et al., Electronics system for the cosmic X-ray polarization detector. Nucl. Sci. Tech. **34**, 64 (2023). https://doi.org/10.1007/s41365-023-01221-3
34. X. Huang, H. Liu, J. Zhang et al., Simulation and photoelectron track reconstruction of soft X-ray polarimeter. Nucl. Sci. Tech. **32**, 67 (2021). https://doi.org/10.1007/s41365-021-00903-0
35. Z. Li, H. Feng, X. Huang et al., Preliminary test of topmetal-II- sensor for X-ray polarization measurements. Nucl. Instrum. Methods Phys. Res. Sect. A **1008**, 165430 (2021). https://doi.org/10.1016/j.nima.2021.165430
36. M. Minuti, L. Baldini, R. Bellazzini et al., XPOL-III: A new-generation VLSI CMOS ASIC for high-throughput X-ray polarimetry. Nucl. Instrum. Methods Phys. Res. Sect. A **1046**, 167674 (2023). https://doi.org/10.1016/j.nima.2022.167674
37. A. Roberts, P. Svihra, A. Al-Refaie et al., First demonstration of 3D optical readout of a TPC using a single photon sensitive Timepix3 based camera. JINST **14**, P06001 (2019). https://doi.org/10.1088/1748-0221/14/06/P06001
38. M. Huang, H. Pei, X. Sun et al., Simulation study of energy resolution with changing pixel size for radon monitor based on Topmetal-II- TPC. Nucl. Sci. Tech. **30**, 16 (2019). https://doi.org/10.1007/s41365-018-0532-8
39. R. Bellazzini, F. Angelini, L. Baldini et al., Gas pixel detectors for X-ray polarimetry applications. Nucl. Instrum. Methods Phys. Res. Sect. A **560**, 425–434 (2006). https://doi.org/10.1016/j.nima.2006.01.046
40. R. Bellazzini, G. Spandre, M. Minuti et al., A sealed Gas Pixel Detector for X-ray astronomy. Nucl. Instrum. Methods Phys. Res. Sect. A **579**, 853–858 (2007). https://doi.org/10.1016/j.nima.2007.05.304
41. R. Bellazzini, L. Baldini, A. Brez et al., Gas pixel detectors. Nucl. Instrum. Methods Phys. Res. Sect. A **572**, 160–167 (2007). https://doi.org/10.1016/j.nima.2006.10.171
42. H. Feng, W. Jiang, M. Minuti et al., PolarLight: a CubeSat X-ray polarimeter based on the gas pixel detector. Exp. Astronom. **47**, 225–243 (2019). https://doi.org/10.1007/s10686-019-09625-z
43. L. Baldini, M. Barbanera, R. Bellazzini et al., Design, construction, and test of the gas pixel detectors for the IXPE mission. Astro. Phys. **133**, 102628 (2021). https://doi.org/10.1016/j.astropartphys.2021.102628